Title: Snapshots of acetyl-CoA synthesis, the final step of CO_2 fixation in the Wood-Ljungdahl pathway

Authors: Max Dongsheng Yin[1]†, Olivier N. Lemaire[2]†, José Guadalupe Rosas Jiménez[3,4], Mélissa Belhamri[2], Anna Shevchenko[5], Gerhard Hummer[3]*, Tristan Wagner[2]*, Bonnie J. Murphy[1]*

Affiliations:

[1] Redox and Metalloproteins Research Group, Max Planck Institute of Biophysics; Max-von-Laue-Straße 3, 60438 Frankfurt am Main, Germany.

[2] Max Planck Research Group Microbial Metabolism, Max Planck Institute of Marine Microbiology; Celsiusstraße 1, 28359 Bremen, Germany.

[3] Department of Theoretical Biophysics, Max Planck Institute of Biophysics; Max-von-Laue-Straße 3, 60438 Frankfurt am Main, Germany.

[4] Department of Theoretical Biophysics, IMPRS on Cellular Biophysics; Max-von-Laue-Straße 3, 60438 Frankfurt am Main, Germany.

[5] Max Planck Institute of Molecular Cell Biology and Genetics; Pfotenhauerstraße 108, 01307 Dresden, Germany.

*To whom correspondence should be addressed:

Bonnie Murphy
bonnie.murphy@biophys.mpg.de
+49 69 6303 3210
ORCID 0000-0001-6341-9368

Tristan Wagner
twagner@mpi-bremen.de
+49 421 2028 7440
ORCID 0000-0002-3382-8969

Gerhard Hummer
gerhard.hummer@biophys.mpg.de
+49 69 6303 2501
ORCID 0000-0001-7768-746X

†These authors contributed equally to this work.

ABSTRACT

In the ancient microbial Wood-Ljungdahl pathway, CO_2 is fixed in a multi-step process ending with acetyl-CoA synthesis at the bifunctional carbon monoxide dehydrogenase/acetyl-CoA synthase complex (CODH/ACS). Here, we present catalytic snapshots of the CODH/ACS from the gas-converting acetogen *Clostridium autoethanogenum*, characterizing the molecular choreography of the overall reaction including electron transfer to the CODH for CO_2 reduction, methyl transfer from the corrinoid iron-sulfur protein (CoFeSP) partner to the ACS active site and acetyl-CoA production. Unlike CODH, the multidomain ACS undergoes large conformational changes to form an internal connection to the CODH active site, accommodate the CoFeSP for

2

methyl transfer and protect the reaction intermediates. Altogether, the structures allow us to draw a detailed reaction mechanism of this enzyme crucial for CO_2 fixation in anaerobic organisms.

One-Sentence Summary: Structural description of key states of CO_2 fixation by the carbon monoxide dehydrogenase/acetyl-CoA synthase complex.

Main Text:

Considered the most ancient and energy-efficient pathway for carbon dioxide (CO_2) fixation, the Wood-Ljungdahl pathway (WLP), also known as the reductive acetyl-coenzyme A (acetyl-CoA) pathway, is responsible for 20% of annual carbon fixation (*1, 2*). The strictly anaerobic process, performed by a wide range of microbes (*e.g.*, acetogenic bacteria and methanogenic archaea) (*3*), is currently applied in gas-mitigation, biotechnologies and biofuel production (*4, 5*). The pathway consists of two branches: the methyl branch, which transforms CO_2 into a methyl group bound to a cobalamin derivative (simplified as B12 below), and the carbonyl branch, where CO_2 is reduced to carbon monoxide (CO). The latter reaction is catalyzed by an Fe-[Ni-3Fe-4S] cluster (C-cluster) in the carbon monoxide dehydrogenase subunit of the bifunctional carbon monoxide dehydrogenase/acetyl-CoA synthase complex (CODH/ACS) (*6-16*). The branches converge on the Ni-Ni-[4Fe-4S] cluster (A-cluster) localized in the ACS subunit (Fig. 1) to generate acetyl-CoA from CO, the methyl group, and CoA (*7, 8, 17*). Depending on the metabolism, acetyl-CoA can be converted to acetate for energy conservation, or assimilated into cell carbon (*18, 19*). Alternatively, other microbes utilize the same enzyme for the reverse process of acetyl-CoA decarbonylation (*10, 20*).

Structural insights into the catalytic reactions of CODH and ACS have been obtained from standalone enzymes and bifunctional CODH/ACS complexes from *Moorella thermoacetica, Carboxydothermus hydrogenoformans* and *Clostridium autoethanogenum* (*Mt, Ch and Ca*, respectively) (*7, 8, 11, 14-17, 21, 22*). However, the overall molecular mechanism of acetyl-CoA synthesis is still not fully understood due to the complexity of the reaction, which requires several additional actors and substantial structural rearrangements of the ACS.

In one of the accepted scenarios, the reaction initiates with the CO_2 reduction at the C-cluster, which requires electron transfer from a ferredoxin (*23*). The electrons are first transferred to a solvent-exposed [4Fe-4S] cluster (D-cluster, alternatively a [2Fe-2S] cluster) (*6, 11, 24-26*) located on the symmetrical axis of the CODH dimer, before being transferred to the C-cluster through an intermediate [4Fe-4S] cluster (B-cluster). Once produced, CO is channeled to the A-cluster through a hydrophobic internal tunneling network and covalently binds as a carbonyl group to the proximal Ni (Ni_p) (*7, 15, 21, 27*). Subsequently, the methyl-Co(III)-B12, carried by the corrinoid iron-sulfur protein (CoFeSP), interacts with the carbonylated ACS to perform methyl transfer. The methyl and carbonyl groups react to generate an acetylated A-cluster (*28*), which promotes the formation of acetyl-CoA through its reaction with the thiol group of CoA.

This reaction mechanism requires flexibility of the ACS as a prerequisite for complete turnover, as the ACS must undergo sequential reactions dependent on ferredoxin, gas trafficking, CoFeSP and CoA. The ACS is composed of three functional domains (A1, A2, and A3, from N- to C-terminus) separated by linkers that allow interdomain flexibility. Multiple conformational arrangements of the ACS have been shown through X-ray crystallography and negative-stain electron microscopy (*7, 8, 14-17, 22, 29*). However, high-resolution structures of the CODH/ACS complex with its partners or ligands are lacking.

In this study, we aimed to capture the CODH/ACS in action by visualizing the missing conformations under various protein-protein interaction or ligand-binding conditions. All presented results are derived from proteins anaerobically isolated from the biotechnologically relevant syngas converter *C. autoethanogenum*, an acetogen that we cultivate heterotrophically on

fructose and H_2/CO_2 as reported previously (*15*). Previous studies have shown that CODH/ACS from *C. autoethanogenum* catalyzes the reversible CO oxidation with artificial electron acceptors or ferredoxin as the physiological partner, methylates the A-cluster with methyl-cobinamide (*15, 30, 31*). To structurally characterize the mechanism of acetyl-CoA synthesis, a 1:2:1 mixture of CODH/ACS heterotetramer, CoFeSP, and ferredoxin, all identified by mass spectrometry ((*15, 30*), fig. S1), was incubated with iodomethane as methyl donor and CO as carbonyl and electron donor. This mixture was plunge-frozen for cryo-EM analysis under anaerobic conditions at ~5% CO in the gas phase. After electron microscope imaging and initial data processing, we performed three-dimensional (3D) refinement with C_2 symmetry, yielding maps of the rigid core of the enzyme, composed of the CODH and A1, at resolutions reaching 1.94 Å (figs. S2-3, tables S1-2). By further classifying the CODH/ACS into different states, we gain a detailed view of acetyl-CoA synthesis.

Ferredoxin-dependent CO_2-reduction at the C-cluster

The less well-resolved density observed at the symmetry axis of CODH was further analyzed by focused classification and local refinement without symmetry applied, resulting in a map showing a ferredoxin harboring two [4Fe-4S] clusters bound asymmetrically near the D-cluster on the C_2 symmetry axis (Fig. 2A, figs. S3B, S4 and S5A). The partial occupancy of ferredoxin and its high b-factors reflect the expected transient interaction. Hydrogen bonding and hydrophobic contacts stabilize the complex (fig. S5B), forming an interaction network that could be supplemented by electrostatic attraction between positively charged residues (Lys35, Lys63) on the flexible loops of the CODH and the negatively charged area of the ferredoxin (fig. S5C). While a previous study questioned the role of the D-cluster as an electron entry/exit point due to its midpoint potential in the monofunctional CODH of *Rhodospirillum rubrum* (*23, 32*), the observed interaction and the inter-cluster distance of 8.7 Å in our structure supports ferredoxin docking and electron transfer at the D-cluster (Fig. 2A) (*6, 11, 24-26, 33*). Electrons are then transferred via the B-cluster to the catalytic C-cluster, the density of which suggests no additional ligand on the structure (fig. S6A). An initial model of the C-cluster exhibited a short (2.3 Å) distance between Ni and the pendant iron (Fe_u), both refined with partial occupancy (~50% and ~60-70%, respectively). This led us to conduct mixed quantum mechanics/molecular mechanics (QM/MM) calculations using density functional theory (DFT) for the quantum region. The analysis showed that compared to the oxidized state of the C-cluster, the Ni-Fe_u distance decreases in the 2-electron and 4-electron reduced states $C_{red1(-OH)}$ and $C_{red2(-OH)}$, with the minimal distance predicted as 2.44 Å in the $C_{red2(-OH)}$ (figs. S7-8; table S3). In a topological analysis of the electron density, the emergence of a bond critical point between Ni and Fe_u further indicates the formation of a metal-metal bond in the reduced states (fig. S8D-F). A shortened Ni-Fe_u distance was also shown in the cyanide-bound CODH crystal structure (*34*). By contrast, in the oxidized state, Ni and Fe_u are part of a ring formed by Ni-[Cys523]S-Fe-S. These results suggest that two electrons are stored in the metal-metal (Ni-Fe_u) bond of the C-cluster, as previously proposed (*35*). However, we caution that the low occupancy of the metals and putative mixture of oxidation states of the C-cluster in our sample may require further structural and spectroscopic characterization. Therefore, we model the cluster with an averaged Ni-Fe_u distance of 2.50 Å, a still relatively short distance compared to the previous structures of the enzyme and homologues (fig. S6B-C).

Conformational spectrum of ACS allows A-cluster carbonylation

Poorly resolved density was present at the expected positions of domains A2 and A3. Using focused classification and refinement of symmetry-expanded datasets (fig. S9), we were able to separate two classes (named Class 1 and 2 in the processing workflow, refined to resolutions of 2.83 Å and 3.29 Å, respectively) with clear density for A2 and A3 but without additional density attributed to CoFeSP (figs. S3C-D, S9-10 and tables S2, S4). The rearrangement of the domains can be modeled as multi-body motion (*29*) with very low root mean square deviation (RMSD) of each domain across different conformational states and organisms (table S5). Multiple terms have been used to describe the ACS conformation in previous works, such as 'open', 'closed' and 'extended'. Here, we introduce a reference framework for a simple comparison of these states in terms of distances between conserved sites in the three domains. In addition to the global opening/closing of the ACS due to a highly flexible loop connecting A1 to A2 (previously shown to be highly sensitive to limited proteolysis (*15*)), the A2-A3 part can potentially perform an opening-closing movement as well, allowing or occluding access to the Ni_p independently of the A1 position. To best characterize this dual flexibility, we propose the distances Ni_p-F209 and F491-W405 (*Ca*ACS numbering) as proxies of interdomain 1-3 and interdomain 2-3 spacing, respectively (L_{1-3} and L_{2-3}, where 'L' stands for 'length').

The *Ca*ACS class 1 resembles the closed conformation of *Mt*CODH/ACS and *Ch*CODH/ACS (*7, 8, 14, 16*), featuring a short L_{1-3} and a long L_{2-3} (Fig. 2B, figs. S11A and S12, table S6). In the closed state, the A2-A3 space is opened and the A-cluster apposes A1 surface. A predicted CO channel emanating from the C-cluster opens into a solvent-occluded space around the A-cluster (*27*). In this state, an additional density observed on Ni_p is modeled as a CO bound to the tetrahedral Ni (fig. S13A-B). Well-conserved hydrophobic residues Val125, Phe209, and Phe491 are positioned similarly to their counterparts in the CO-bound state of *Mt*CODH/ACS (*14*) (fig. S13B-C). These residues were proposed to stabilize the tetrahedral geometry of the carbonylated Ni_p, facilitate CO diffusion through internal cavities to the A-cluster, and hinder the A-cluster from adopting a methylation-compatible geometry (*14*).

By contrast, the class 2 corresponds to the semi-extended state previously described in the crystallographic structure of *Ca*CODH/ACS (PDB 6YTT, chain D) (*15*) (Fig. 2B, fig. S11B). In this state, the A3 is disengaged from the A1 and the Ni_p is occluded by the closing of A2-A3 (fig. S12A). The resolution is too limited to describe a bound ligand on the A-cluster (carbonyl or methyl). Class 2 likely reflects a conformation en route towards CoFeSP docking, protecting the Ni_p to avoid side reactions while gradually opening the interdomain A1-A3 space (table S6).

CoFeSP interaction promotes the ACS hyper-extended state

Focused classification of the flexible ACS unveiled a third class corresponding to the CODH/ACS-CoFeSP complex (Fig. 2B, figs. S9-10, S14 and tables S2, S4). Compared to the extended state obtained by crystallography (PDB 6YTT, chain A) (*15*), ACS complexed with CoFeSP maintains a long L_{1-3} and additionally opens L_{2-3} via a 59° rotation of A3, leading to a hyper-extended state (figs. S12C and S15; table S6). Consequently, this is the sole state obtained in our study in which the A-cluster is fully accessible for methyl transfer.

The hyper-extension is maintained by three anchoring points: docking of the CoFeSP small subunit to both A1 and A3 and the interaction between the [4Fe-4S] cluster domain of the CoFeSP large subunit (1-57) and the A3 (figs. S16-17). The [4Fe-4S] cluster domain, and to a lesser extent the B12-binding domain (CoFeSP large subunit, 326-446), show the most structural differences when

compared to structural homologues in complex with the activator protein or the methyltransferase (MeTr) (fig. S18) (*36, 37*). The distance between the [4Fe-4S] cluster and the A-cluster (32.3 Å, fig. S17) precludes electron transfer, agreeing with previous studies indicating no direct involvement of the CoFeSP [4Fe-4S] cluster in ACS methylation (*38, 39*). Our findings rather support the function of this domain in stabilizing the hyper-extended ACS and its interaction with CoFeSP, similar to its role during interactions with the activator protein or the MeTr (fig. S18) (*36, 37*). Residues involved in the interaction between ACS and CoFeSP are mostly conserved among bacteria and archaea (figs. S16-17), suggesting a similar mode of action across microbial kingdoms.

Methyl transfer reaction through B12 domain motion

The hyper-extended state of the ACS enables the bulky CoFeSP to access the A-cluster ('class 3'; Fig. 2B and Fig. 3), but additional motion of the CoFeSP is required to bring the B12 close enough for methyl transfer (*37, 40*). Via 3D variability analysis (3DVA) of the class 3, we resolve a rotational motion of the B12-binding domain (Fig. 3B). Supervised classification using three intermediate reconstructions from 3DVA led to three subsets (3A, 3B and 3C), with 3A and 3B refined to 2.71 Å and 2.65 Å, respectively (table S2). The subset 3C appeared as a mixture of two states, with the corrinoid group density stretching further towards Ni_p (fig. S19). By building preliminary models for each configuration and using their corresponding molmaps for supervised classification of class 3C, we obtained two substates, 3Cα and 3Cβ, refined to 2.78 Å and 2.88 Å, respectively (table S2). These maps represent snapshots of the rotational motion, during which the B12 approaches Ni_p (Fig. 3, movie S1), reminiscent of the motion described in the *Mt*CoFeSP complexed with its MeTr (*37*). In the 3A/3B/3Cβ sequential movement, the B12 ring progressively breaks all hydrogen bonds with the CoFeSP and establishes new ones with the ACS (Fig. 3C). These conserved hydrogen-bonding residues stabilize the B12 as it moves towards the A-cluster, with the shortest Co-Ni_p distance of 6.7 Å observed in 3Cβ (Fig. 3B-D), nearly sufficient for direct methyl transfer. We suppose that a transient state exists with a further shortened distance suitable for methyl transfer, as in the CoFeSP-MeTr, but this state appears too rare to be captured via classification or 3DVA. No obvious density for a methyl or carbonyl group could be detected at either the corrinoid or the Ni_p site. We assessed the possibility of ligand loss due to radiation damage at the site by reconstructing only early frames, corresponding to as little as 3.7 MGy (*41*), but did not observe notable differences in the density (fig. S20A).

For the states containing no external ligand at Ni_p, our refined models consistently exhibited relatively short distances between the Ni_p and S1 sulfide of the [4Fe-4S] cluster (fig. S20B). To test the chemical feasibility of this configuration, we carried out a QM/MM analysis (fig. S7), using the best-resolved structure, *i.e.*, class 3B. Our calculations suggested that, in the absence of a fourth ligand bound to Ni^+, a strong attractive interaction with the [4Fe-4S] cluster brings Ni_p into bonding distance (S21A; table S7). The topological analysis of the electron density reveals a bond critical point and a corresponding bond path connecting one of the sulfides in the cubane and the Ni_p cation (fig. S21B). A ring critical point is found between one of the Fe-S edges of the cluster and the Cys488-Ni_p bond, forming a 4-membered ring resembling one of the faces of the cubane. Previous experimental and theoretical studies proposed significant rearrangements between tetrahedral and square planar geometries during catalysis (*42*). Based on our calculations, it is feasible that a low-valent Ni_p is coordinated by a sulfide of the [4Fe-4S] cluster, generating the extended cubane structure observed in the experiment. Upon ligand binding, a four-coordinated Ni complex can form, recovering the usual geometry proposed for other reaction intermediates.

Therefore, the Ni_p geometry modeled in our cryo-EM structures is consistent with the apparent absence of density for ligands, even though a low occupancy (~45-59%) of the Ni_p site, the relatively low resolution and the putatively mixed state may hamper the accurate determination of the Ni_p geometry and the detection of ligands.

The acetyl-CoA complex, a snapshot of the bound reaction product

Carbonyl and methyl groups bound at Ni_p combine to form an acetyl (*28*), which is subsequently transferred to the thiol group of CoA. Despite our efforts, we could not unambiguously detect additional cryo-EM map density in CODH/ACS treated with CoA or acetyl-CoA. However, by co-crystallizing *Ca*CODH/ACS with acetyl-CoA, we obtained a 2.93 Å X-ray structure of the product-bound complex (CODH/ACS$_{AC}$, table S8). The global conformations resemble those of the as-isolated *Ca*CODH/ACS (*15*) (fig. S22). However, the previously semi-extended ACS now exhibits additional density spanning the A2 surface and reaching A3, modeled as acetyl-CoA, while the extended ACS of the asymmetric unit lacks such density, reflecting the strict conformational requirement for ligand binding (Fig. 4, fig. S23).

The acetyl-CoA primarily interacts with A2 residues, with the adenine group stabilized by Trp405 via π-stacking, and the diphosphate facing a positively charged patch rich in lysines and arginines (Fig. 4, fig. S24A). The relatively high b-factors of the adenosine diphosphate moiety (fig. S24B) indicate only partial stabilization of the acetyl-CoA in the A2-A3 cleft that is restrained by the crystalline packing.

Compared to the ligand-free semi-extended ACS resolved by cryo-EM, acetyl-CoA-bound ACS undergoes a 15° rotation of A3 (fig. S25A). This further stabilizes acetyl-CoA binding via additional contacts with the A3 (Fig. 4), resolves potential clashes between A3 and acetyl-CoA (fig. S23B), and brings the A-cluster into closer proximity of the acetyl-CoA (fig. S25A). In this state, the acetyl-bearing sulfur atom is 4.13 Å away from the Ni_p, with the acetyl group stabilized by the hydrogen-bonding with the main chain of Gly399 for the carbonyl moiety, and interaction with the His386 for the methyl moiety (Fig. 4). The flexible Phe491 swings away from the Ni_p (fig. S25B) to avoid steric hindrance to the CoA attack. The conserved Arg383 and His386, located near the A-cluster in the structure (Fig. 4), are likely crucial for acetyl transfer. Superposition with an acetylated A-cluster structure from a previous DFT study (*43*) indicates that Arg383 would be in the direct vicinity of the Ni_p-bound acetyl group, putatively stabilizing it via H-bonding (fig. S25C). His386 is well positioned in our structure to facilitate deprotonation of the thiol group (Fig. 4B), consistent with previous analysis (*17*). The majority of the residues involved in acetyl-CoA stabilization in the CODH/ACS$_{AC}$ were already suggested in *Mt*ACS (*17*), and most of these interacting residues are conserved among bacteria and archaea (Fig. 4), which suggests a strong evolutionary pressure to avoid possible clashes during the overall catalysis.

Discussion

By providing new structural insights into the electron transfer, methyl transfer, and acetyl-CoA formation steps, our work advances decades of studies on the catalytic cycle of the CODH/ACS. The study illustrates the elegant and intricate reaction mechanism of this key anaerobic CO_2 fixation machinery, which exhibits a wide range of ACS conformations relying on interdomain flexibility, as proposed by previous studies (*23, 29*). To simplify the nomenclature and comparison

of these conformations, we introduce new metrics based on the interdomain distances L_{1-3} and L_{2-3}, enabling the clustering of conformational states in a 2D landscape (Fig. 5A, table S6). The landscape generated from structurally characterized ACS allows us to construct a conformation-based model of the overall reaction of the CODH/ACS (Fig. 5B). In a sequential carbonylation-methylation scenario, the reaction would initiate in a closed state. Ferredoxin docking on the D-cluster and the subsequent electron transfer drive the CO formation, which can diffuse from the C-cluster to the A-cluster (*14*) for Ni_p carbonylation. The methylation step would require a hyper-extended configuration to accommodate the methyl donor CoFeSP, involving a movement of more than 37 Å of the A-cluster (fig. S26). During the movement (increasing L_{1-3}), the A-cluster-carrying A3 must be undocked from the A1, which could leave the reactive carbonyl-Ni_p site exposed. This appears to be mitigated by closing of L_{2-3} in the semi-extended and extended states (Fig. 5A, fig. S12A-B), which shelters the A-cluster. Upon binding of CoFeSP, the hyper-extended state is stabilized, characterized by its long distance L_{2-3} and exposed A-cluster (Figs. 2B and 5A, fig. 12C and table S6). The B12 domain of CoFeSP 'waltzes' toward this open space, positioning the B12 close enough for the methyl transfer. After reaction of the carbonyl and methyl groups to a Ni_p-bound acetyl group, the ACS would release the CoFeSP. Although CoA primarily interacts with A2, it must be brought near the A-cluster on A3 to further stabilize the binding and initiate acetyl transfer. Thus, acetyl-CoA formation appears to require a return to shorter L_{2-3}, where A3 is rotated relative to the semi-extended state to finely tune the cleft between A2 and A3 for the nucleophilic attack of the thiol group of CoA (fig. S25A). After acetyl-CoA release, the ACS returns to the closed conformation for another catalytic cycle.

The proposed scenario does not exclude a reverse sequential order, *i.e.*, a sequential methylation-carbonylation process. A specific reaction order is perhaps not required, since the ACS exhibits a wide conformational spectrum in solution (Fig. 2B). We note that among all characterized *Ca*ACS structures obtained by cryo-EM from the same sample, a carbonyl ligand is observed only in the closed state, although this could also be due to experimental limitations.

The overall architecture of *Ca*CODH/ACS differs from the model *Mt*CODH/ACS or *Ch*CODH/ACS (*15*). However, aligning all reported *Ca*ACS conformation to the rigid A1 (N-terminal domain) of *Mt*ACS shows no clashes with the rigid core of *Mt*CODH. This suggests that the conformational states and reaction mechanism described here could be generalized to complexes including *Mt*CODH/ACS and *Ch*CODH/ACS, in which the N-terminal domain of ACS forms different contacts with the CODH dimer (fig. S27).

To complete the reaction landscape of ACS, several intermediate structures are still needed, including methyl-bound, CO- and methyl-bound, acetyl-bound and CoA-bound ACS. These snapshots could elucidate the mechanisms underlying the triggering or regulation of the conformational transitions, which is crucial for this reversible and central enzyme in the global carbon cycle.
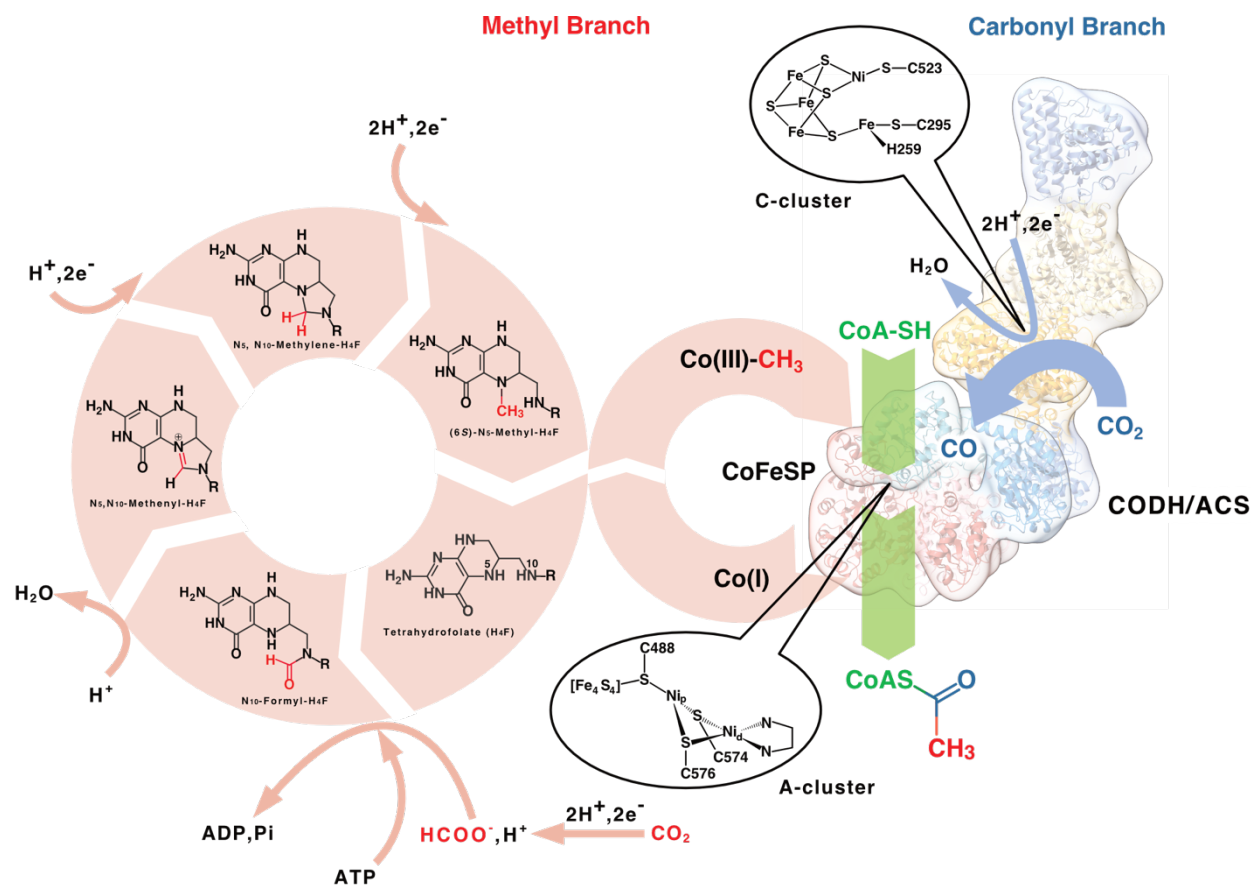
Fig. 1. The Wood-Ljungdahl pathway. One molecule of CO_2 is reduced in the multi-step methyl branch (pink arrows), while another is reduced at the C-cluster of CODH in the carbonyl branch (light blue arrows). The methyl and carbonyl moieties react, and the acetyl group is transferred as a thioester of coenzyme A, at the A-cluster of ACS (green arrows). For simplicity, only the bacterial WLP is depicted. The reverse decarbonylation process and the archaeal equivalent pathway are not shown. The latter depends on analogous reactions, with tetrahydromethanopterin replacing H_4F and a formate condensation reaction being independent of ATP hydrolysis as major differences (*3*).

9
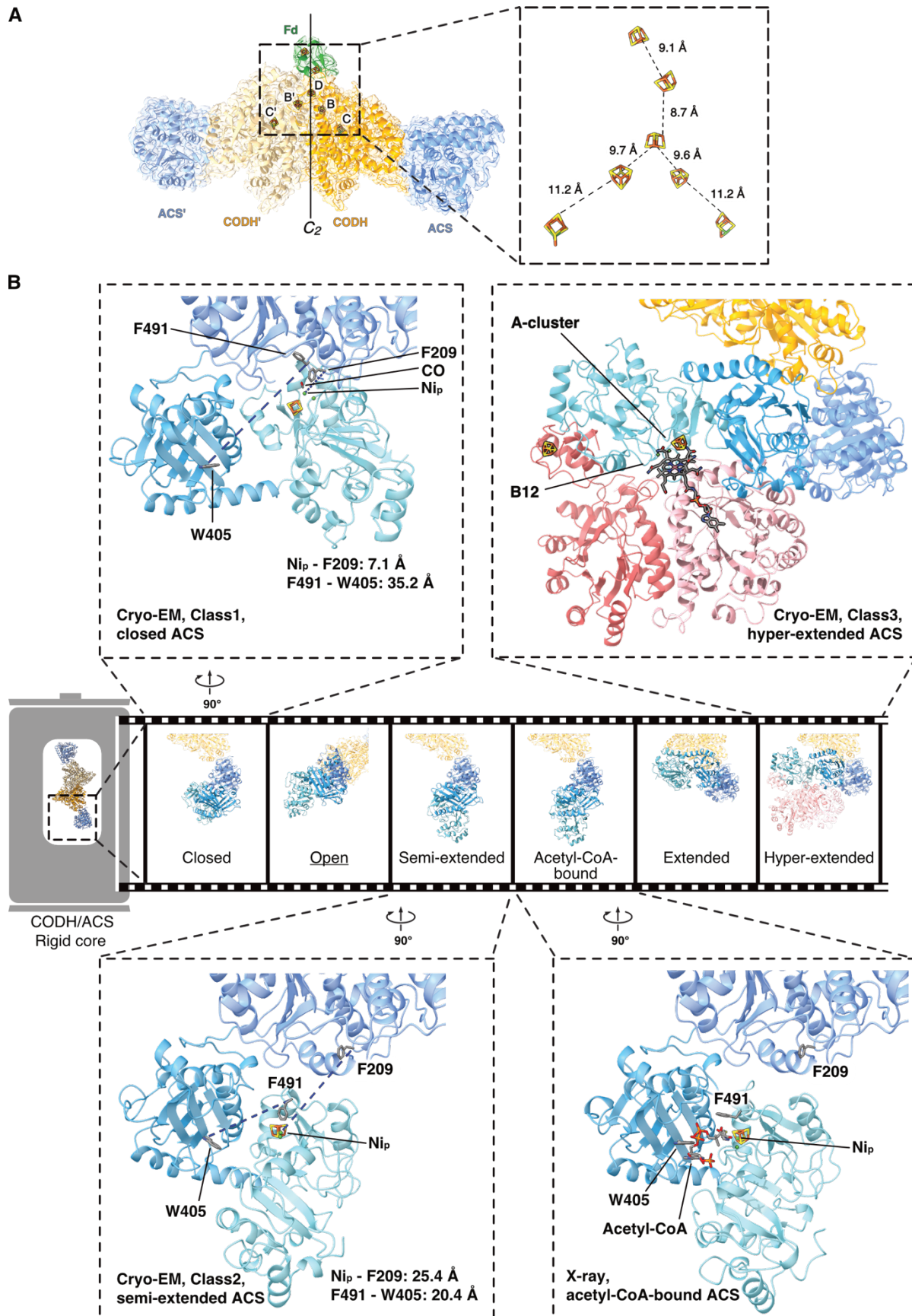
Fig. 2. Conformational gallery of the CODH/ACS. (**A**) Ferredoxin (forest green) docks at the C_2 symmetry axis of CODH (gold/wheat). The symmetry axis is indicated with a vertical line. Inset: the binding conformation should allow efficient electron transfer between the [4Fe-4S] cluster of ferredoxin and the D-cluster of CODH; distances are shown as dashed lines. (**B**) The collection of flexible ACS conformations, with structures from the current study highlighted and aligned according to the A1 domain with the open state obtained from *Mt*CODH/ACS (underlined, PDB 1OAO, chain D) and the extended state (*Ca*CODH/ACS, PDB 6YTT, chain A) of ACS. The domains of ACS are shown in shades of blue, from darker at the N-terminus to lighter at the C-terminus. The Ni_p-F209 and F491-W405 distances for the closed and semi-extended states are indicated by dashed lines, with the measured values provided alongside the structures. ACS adopts a hyper-extended state to allow binding of the methyl-donor protein CoFeSP (pink). In the hyper-extended state, the Ni_p-F209 and F491-W405 distances are 39.8-40.5 Å and 36.8-39.4 Å, respectively, whereas in the acetyl-CoA-bound ACS, these distances are 26.7 Å and 14.9 Å, respectively (table S6). All metallocofactors are in stick representation and colored according to the element.
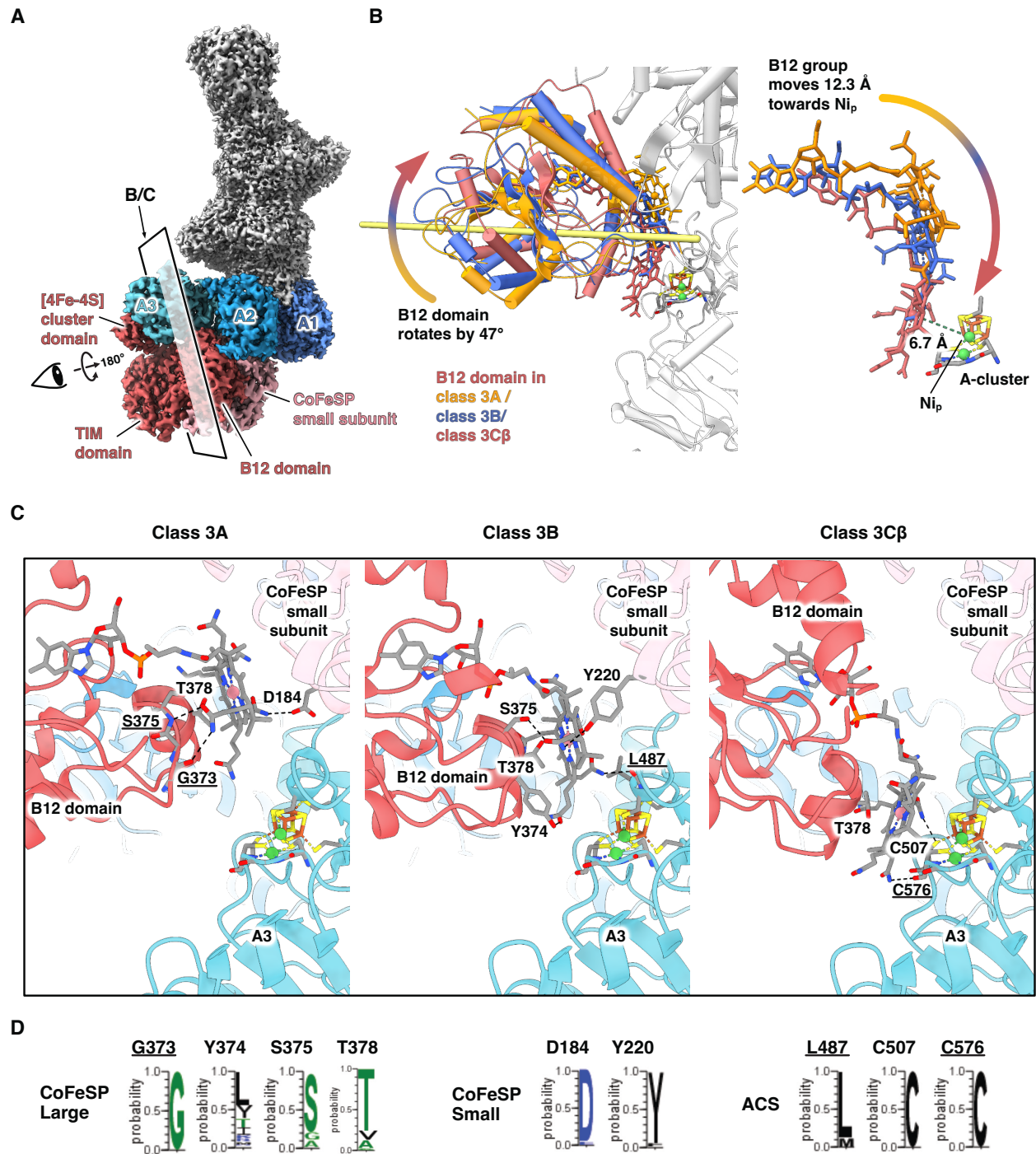
11

Fig. 3. In the hyper-extended, CoFeSP-bound state, rotation of the CoFeSP B12 domain brings the B12 toward the Ni_p. (**A**) The cryo-EM map, with the ACS in complex with a CoFeSP colored according to the established color scheme established in Fig. 2, while the rest of the complex is in gray. (**B**) The B12 domain undergoes a 47° rotation (rotation axis as a light-yellow stick) from class 3A to class 3Cβ, positioning the Co atom of B12 6.7 Å away from the Ni_p. The B12 domain and B12 are colored according to the rotational states, and the rest of the complex is in gray. (**C**) Detailed views of the three rotational states, with key hydrogen bonds indicated by dashed lines. (**D**) Sequence conservation analysis shows that most of the B12-stabilizing residues are well conserved in bacteria and archaea. In both (C) and (D), residues involved in hydrogen-bonding via their main chain atoms are underlined.
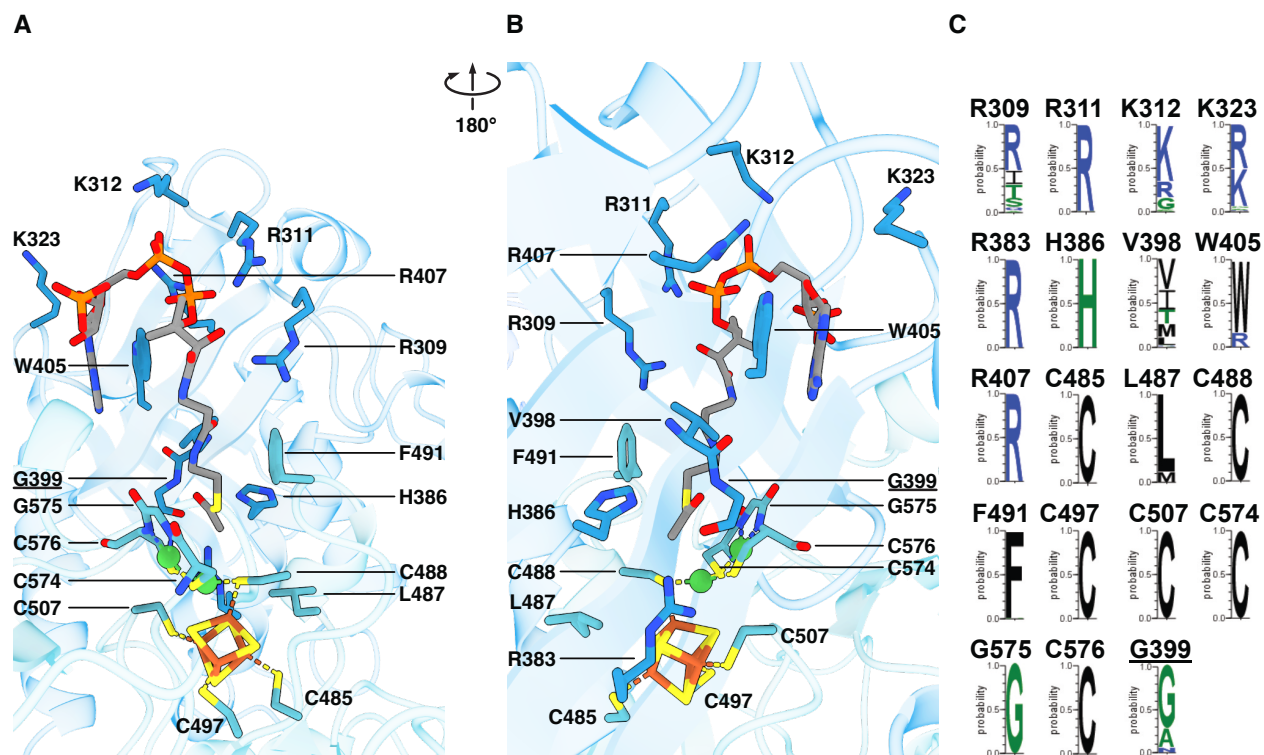
Fig. 4. CODH/ACS in the acetyl-CoA bound state. (A-B) Close-up views of acetyl-CoA binding, highlighting the key residues involved in the interaction. **(C)** Conservation of the residues in bacteria and archaea. Residues involved in hydrogen-bonding via their main chain atoms are underlined.
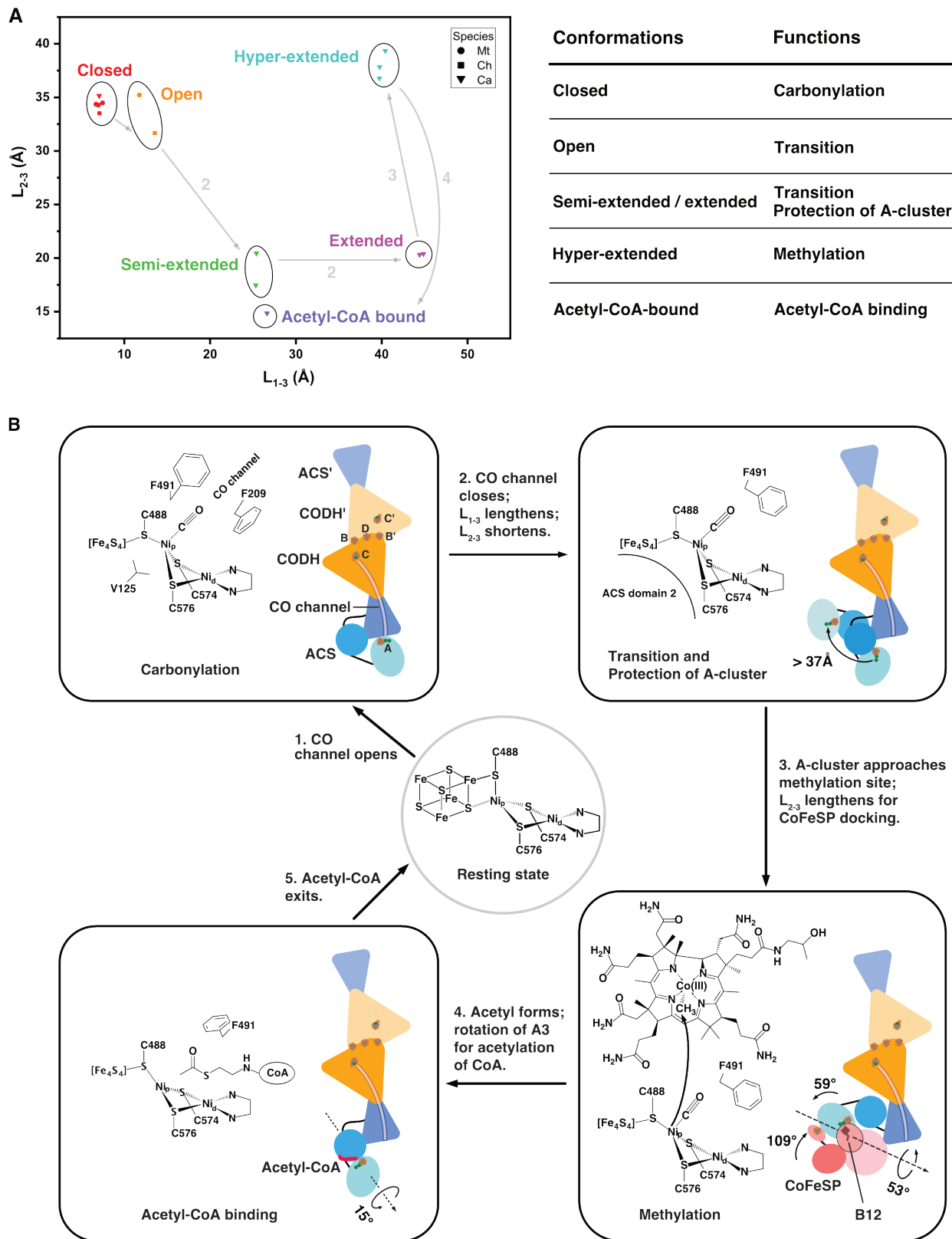
A

Conformations	Functions
Closed	Carbonylation
Open	Transition
Semi-extended / extended	Transition Protection of A-cluster
Hyper-extended	Methylation
Acetyl-CoA-bound	Acetyl-CoA binding

B

15

Fig. 5. A conformation-based model of acetyl-CoA synthesis. (**A**) The conformational 2D spectrum of all known structures of CODH/ACS. One proposed reaction route, starting with carbonylation, is marked by arrows and numbered according to the model in (B). The function of each conformation is summarized in the table. (**B**) A proposed mechanism of acetyl-CoA synthesis in the sequential carbonylation-methylation scenario. Schematic representation of key CODH/ACS conformations with their functional roles, as well as the corresponding configurations of the A-cluster, are presented in the boxes. The reaction route is labeled with solid arrows, while critical domain motions during the reaction are marked by curved arrows and further illustrated in figs. S15, S18, S25A and S26. In the ligand-free resting state, the feasible Ni_p-S coordination is indicated by a gray stick.

16

References:

1. G. Fuchs, Alternative pathways of carbon dioxide fixation: insights into the early evolution of life? *Annual Reviews in Microbiology* **65**, 631-658 (2011). https://doi.org/10.1146/annurev-micro-090110-102801

2. L. G. Ljungdahl, A life with acetogens, thermophiles, and cellulolytic anaerobes. *Annual Reviews in Microbiology* **63**, 1-25 (2009). https://doi.org/10.1146/annurev.micro.091208.073617

3. O. N. Lemaire, M. Jespersen, T. Wagner, CO_2-Fixation Strategies in Energy Extremophiles: What Can We Learn From Acetogens? *Frontiers in Microbiology* **11**, 486 (2020). https://doi.org/10.3389/fmicb.2020.00486

4. J. K. Heffernan *et al.*, Enhancing CO_2-Valorization Using *Clostridium autoethanogenum* for Sustainable Fuel and Chemicals Production. *Frontiers in Bioengeneering and Biotechnology* **8**, 204 (2020). https://doi.org/10.3389/fbioe.2020.00204

5. W. Wang, D.-J. Lee, Z. Lei, Integrating anaerobic digestion with microbial electrolysis cell for performance enhancement: A review. *Bioresource Technology* **344**, 126321 (2022). https://doi.org/10.1016/j.biortech.2021.126321

6. C. L. Drennan, J. Heo, M. D. Sintchak, E. Schreiter, P. W. Ludden, Life on carbon monoxide: X-ray structure of *Rhodospirillum rubrum* Ni-Fe-S carbon monoxide dehydrogenase. *Proceedings of the National Academy of Sciences of the United States of America* **98**, 11973-11978 (2001). https://doi.org/10.1073/pnas.211429998

7. T. I. Doukov, T. M. Iverson, J. Seravalli, S. W. Ragsdale, C. L. Drennan, A Ni-Fe-Cu Center in a Bifunctional Carbon Monoxide Dehydrogenase/ Acetyl-CoA Synthase. *Science* **298**, 567-572 (2002). https://doi.org/10.1126/science.1075843

8. C. Darnault *et al.*, Ni-Zn-[Fe_4-S_4] and Ni-Ni-[Fe_4-S_4] clusters in closed and open α subunits of acetyl-CoA synthase/carbon monoxide dehydrogenase. *Nature Structural and Molecular Biology* **10**, 271-279 (2003). https://doi.org/10.1038/nsb912

9. J. H. Jeoung, H. Dobbek, Carbon dioxide activation at the Ni,Fe-cluster of anaerobic carbon monoxide dehydrogenase. *Science* **318**, 1461-1464 (2007). https://doi.org/10.1126/science.1148481

10. W. Gong *et al.*, Structure of the $alpha_2epsilon_2$ Ni-dependent CO dehydrogenase component of the *Methanosarcina barkeri* acetyl-CoA decarbonylase/synthase complex. *Proceedings of the National Academy of Sciences of the United States of America* **105**, 9558-9563 (2008). https://doi.org/10.1073/pnas.0800415105

11. Y. Kung, T. I. Doukov, J. Seravalli, S. W. Ragsdale, C. L. Drennan, Crystallographic Snapshots of Cyanide- and Water-Bound C-Clusters from Bifunctional Carbon Monoxide Dehydrogenase/Acetyl-CoA Synthase. *Biochemistry* **48**, 7432-7440 (2009). https://doi.org/10.1021/bi900574h

12. L. Domnik *et al.*, CODH-IV: A High-Efficiency CO-Scavenging CO Dehydrogenase with Resistance to O_2. *Angewandte Chemie International Edition English* **56**, 15466-15469 (2017). https://doi.org/10.1002/anie.201709261

13. E. C. Wittenborn *et al.*, Redox-dependent rearrangements of the NiFeS cluster of carbon monoxide dehydrogenase. *Elife* **7**, (2018). https://doi.org/10.7554/eLife.39451

14. S. E. Cohen *et al.*, Crystallographic Characterization of the Carbonylated A-Cluster in Carbon Monoxide Dehydrogenase/Acetyl-CoA Synthase. *ACS Catalysis* **10**, 9741-9746 (2020). https://doi.org/10.1021/acscatal.0c03033

15. O. N. Lemaire, T. Wagner, Gas channel rerouting in a primordial enzyme: Structural insights of the carbon-monoxide dehydrogenase/acetyl-CoA synthase complex from the acetogen *Clostridium autoethanogenum*. *Biochimica et Biophysica Acta Bioenergetics* **1862**, 148330 (2021). https://doi.org/10.1016/j.bbabio.2020.148330

16. J. Ruickoldt, Y. Basak, L. Domnik, J. H. Jeoung, H. Dobbek, On the Kinetics of CO_2 Reduction by Ni, Fe-CO Dehydrogenases. *ACS Catalysis* **12**, 13131-13142 (2022). https://doi.org/10.1021/acscatal.2c02221

17. A. Volbeda, C. Darnault, X. Tan, P. A. Lindahl, J. C. Fontecilla-Camps, Novel domain arrangement in the crystal structure of a truncated acetyl-CoA synthase from *Moorella thermoacetica*. *Biochemistry* **48**, 7916-7926 (2009). https://doi.org/10.1021/bi9003952

18. K. Schuchmann, V. Muller, Autotrophy at the thermodynamic limit of life: a model for energy conservation in acetogenic bacteria. *Nature Reviews Microbiology* **12**, 809-821 (2014). https://doi.org/10.1038/nrmicro3365

19. J. Mock *et al.*, Energy Conservation Associated with Ethanol Formation from H_2 and CO_2 in *Clostridium autoethanogenum* Involving Electron Bifurcation. *Journal of Bacteriology* **197**, 2965-2980 (2015). https://doi.org/10.1128/JB.00399-15

20. A. Biester, A. N. Marcano-Delgado, C. L. Drennan, Structural Insights into Microbial One-Carbon Metabolic Enzymes Ni–Fe–S-Dependent Carbon Monoxide Dehydrogenases and Acetyl-CoA Synthases. *Biochemistry* **61**, 2797-2805 (2022). https://doi.org/10.1021/acs.biochem.2c00425

21. T. I. Doukov, L. C. Blasiak, J. Seravalli, S. W. Ragsdale, C. L. Drennan, Xenon in and at the End of the Tunnel of Bifunctional Carbon Monoxide Dehydrogenase/Acetyl-CoA Synthase. *Biochemistry* **47**, 3474-3483 (2008). https://doi.org/10.1021/bi702386t

22. V. Svetlitchnyi *et al.*, A functional Ni-Ni-[4Fe-4S] cluster in the monomeric acetyl-CoA synthase from *Carboxydothermus hydrogenoformans*. *Proceedings of the National Academy of Sciences of the United States of America* **101**, 446-451 (2004). https://doi.org/10.1073/pnas.0304262101

23. M. Can, F. A. Armstrong, S. W. Ragsdale, Structure, function, and mechanism of the nickel metalloenzymes, CO dehydrogenase, and acetyl-CoA synthase. *Chemical Reviews* **114**, 4149-4174 (2014). https://doi.org/10.1021/cr400461p

24. H. Dobbek, V. Svetlitchnyi, L. Gremer, R. Huber, O. Meyer, Crystal structure of a carbon monoxide dehydrogenase reveals a [Ni-4Fe-5S] cluster. *Science* **293**, 1281-1285 (2001). https://doi.org/10.1126/science.1061500

25. J. Chen *et al.*, Infrared studies of carbon monoxide binding to carbon monoxide dehydrogenase/acetyl-CoA synthase from *Moorella thermoacetica*. *Biochemistry* **42**, 14822-14830 (2003). https://doi.org/10.1021/bi0349470

26. E. C. Wittenborn *et al.*, The Solvent-Exposed Fe-S D-Cluster Contributes to Oxygen-Resistance in *Desulfovibrio vulgaris* Ni-Fe Carbon Monoxide Dehydrogenase. *ACS Catalysis* **10**, 7328-7335 (2020). https://doi.org/10.1021/acscatal.0c00934

27. A. Biester, S. Dementin, C. L. Drennan, Visualizing the gas channel of a monofunctional carbon monoxide dehydrogenase. *Journal of Inorganic Biochemistry* **230**, 111774 (2022). https://doi.org/10.1016/j.jinorgbio.2022.111774

28. S. W. Ragsdale, H. G. Wood, Acetate biosynthesis by acetogenic bacteria. Evidence that carbon monoxide dehydrogenase is the condensing enzyme that catalyzes the final steps of the synthesis. *Journal of Biological Chemistry* **260**, 3970-3977 (1985). https://doi.org/10.1016/S0021-9258(18)89217-1

29.   S. E. Cohen *et al.*, Negative-Stain Electron Microscopy Reveals Dramatic Structural Rearrangements in Ni-Fe-S-Dependent Carbon Monoxide Dehydrogenase/Acetyl-CoA Synthase. *Structure* **29**, 43-49.e43 (2021). https://doi.org/10.1016/j.str.2020.08.011

30.   O. N. Lemaire, M. Belhamri, A. Shevchenko, T. Wagner, Carbon monoxide-driven bioethanol production operates via a tungsten-dependent catalyst. *bioRxiv 2024.07.29.605569*, (2024). https://doi.org/10.1101/2024.07.29.605569

31.   S. Wiley *et al.*, An alcove at the acetyl-CoA synthase nickel active site is required for productive substrate CO binding and anaerobic carbon fixation. *J Biol Chem* **300**, 107503 (2024). https://doi.org/10.1016/j.jbc.2024.107503

32.   J. L. Craft, P. W. Ludden, T. C. Brunold, Spectroscopic studies of nickel-deficient carbon monoxide dehydrogenase from *Rhodospirillum rubrum*: nature of the iron-sulfur clusters. *Biochemistry* **41**, 1681-1688 (2002). https://doi.org/10.1021/bi011586k

33.   C. C. Page, C. C. Moser, X. Chen, P. L. Dutton, Natural engineering principles of electron tunnelling in biological oxidation-reduction. *Nature* **402**, 47-52 (1999). https://doi.org/10.1038/46972

34.   J. H. Jeoung, H. Dobbek, Structural basis of cyanide inhibition of Ni, Fe-containing carbon monoxide dehydrogenase. *Journal of American Chemical Society* **131**, 9922-9923 (2009). https://doi.org/10.1021/ja9046476

35.   P. A. Lindahl, Metal-metal bonds in biology. *Journal of Inorganic Biochemistry* **106**, 172-178 (2012). https://doi.org/10.1016/j.jinorgbio.2011.08.012

36.   S. E. Hennig *et al.*, ATP-induced electron transfer by redox-selective partner recognition. *Nature Communications* **5**, 4626 (2014). https://doi.org/10.1038/ncomms5626

37.   Y. Kung *et al.*, Visualizing molecular juggling within a B_{12}-dependent methyltransferase complex. *Nature* **484**, 265-269 (2012). https://doi.org/10.1038/nature10916

38.   S. Menon, S. W. Ragsdale, Role of the [4Fe-4S] cluster in reductive activation of the cobalt center of the corrinoid iron-sulfur protein from *Clostridium thermoaceticum* during acetate biosynthesis. *Biochemistry* **37**, 5689-5698 (1998). https://doi.org/10.1021/bi9727996

39.   S. Menon, S. W. Ragsdale, The role of an iron-sulfur cluster in an enzymatic methylation reaction. Methylation of CO dehydrogenase/acetyl-CoA synthase by the methylated corrinoid iron-sulfur protein. *Journal of Biological Chemistry* **274**, 11513-11518 (1999). https://doi.org/10.1074/jbc.274.17.11513

40.   S. Goetzl, J. H. Jeoung, S. E. Hennig, H. Dobbek, Structural basis for electron and methyl-group transfer in a methyltransferase system operating in the reductive acetyl-CoA pathway. *Journal of Molecular Biology* **411**, 96-109 (2011). https://doi.org/10.1016/j.jmb.2011.05.025

41.   L. A. Baker, J. L. Rubinstein, Radiation damage in electron cryomicroscopy. *Methods in Enzymology* **481**, 371-388 (2010). https://doi.org/10.1016/s0076-6879(10)81015-8

42.   S. Gencic, E. C. Duin, D. A. Grahame, The two-electron reduced A cluster in acetyl-CoA synthase: Preparation, characteristics and mechanistic implications. *Journal of Inorganic Biochemistry* **240**, 112098 (2023). https://doi.org/10.1016/j.jinorgbio.2022.112098

43.   M. Can *et al.*, Characterization of Methyl- and Acetyl-Ni Intermediates in Acetyl CoA Synthase Formed during Anaerobic CO_2 and CO Fixation. *Journal of American Chemical Society* **145**, 13696-13708 (2023). https://doi.org/10.1021/jacs.3c01772

44.   J. G. Rosas-Jiménez *et al.*, QM/MM calculations and geometry optimizations of C- and A-clusters in CODH/ACS, the key enzyme in the Wood-Ljungdahl pathway. Version v1. *Zenodo*, (2024). https://doi.org/10.5281/zenodo.12705281

45.   O. N. Lemaire, Sequence alignments for the determination of residue conservation in ACS, CoFeSP large subunit and CoFeSP small subunit. Version v1. *Zenodo*, (2024). https://doi.org/10.5281/zenodo.12785604

46.   S. Q. Zheng *et al.*, MotionCor2: anisotropic correction of beam-induced motion for improved cryo-electron microscopy. *Nature Methods* **14**, 331-332 (2017). https://doi.org/10.1038/nmeth.4193

47.   D. Kimanius, L. Dong, G. Sharov, T. Nakane, S. H. W. Scheres, New tools for automated cryo-EM single-particle analysis in RELION-4.0. *Biochemical Journal* **478**, 4169-4185 (2021). https://doi.org/10.1042/bcj20210708

48.   A. Rohou, N. Grigorieff, CTFFIND4: Fast and accurate defocus estimation from electron micrographs. *Journal of Structural Biology* **192**, 216-221 (2015). https://doi.org/10.1016/j.jsb.2015.08.008

49.   A. Punjani, J. L. Rubinstein, D. J. Fleet, M. A. Brubaker, cryoSPARC: algorithms for rapid unsupervised cryo-EM structure determination. *Nature Methods* **14**, 290-296 (2017). https://doi.org/10.1038/nmeth.4169

50.   D. Asarnow, Palovcak, E., Cheng, Y., UCSF pyem v0.5. *Zenodo*, (2019). https://doi.org/10.5281/zenodo.3576630

51.   T. Bepler *et al.*, Positive-unlabeled convolutional neural networks for particle picking in cryo-electron micrographs. *Nature Methods* **16**, 1153-1160 (2019). https://doi.org/10.1038/s41592-019-0575-8

52.   D. Liebschner *et al.*, Macromolecular structure determination using X-rays, neutrons and electrons: recent developments in Phenix. *Acta Crystallography section D Structal Biology* **75**, 861-877 (2019). https://doi.org/10.1107/s2059798319011471

53.   K. Jamali *et al.*, Automated model building and protein identification in cryo-EM maps. *Nature*, (2024). https://doi.org/10.1038/s41586-024-07215-4

54.   P. Emsley, B. Lohkamp, W. G. Scott, K. Cowtan, Features and development of Coot. *Acta Crystallography section D Biological Crystallography* **66**, 486-501 (2010). https://doi.org/10.1107/S0907444910007493

55.   J. Jumper *et al.*, Highly accurate protein structure prediction with AlphaFold. *Nature* **596**, 583-+ (2021). https://doi.org/10.1038/s41586-021-03819-2

56.   P. V. Afonine *et al.*, Real-space refinement in PHENIX for cryo-EM and crystallography. *Acta Crystallography section D Structal Biology* **74**, 531-544 (2018). https://doi.org/10.1107/S2059798318006551

57.   K. Yamashita, C. M. Palmer, T. Burnley, G. N. Murshudov, Cryo-EM single-particle structure refinement and map calculation using Servalcat. *Acta Crystallogr D Structal Biology* **77**, 1282-1291 (2021). https://doi.org/10.1107/S2059798321009475

58.   K. Yamashita, M. Wojdyr, F. Long, R. A. Nicholls, G. N. Murshudov, GEMMI and Servalcat restrain REFMAC5. *Acta Crystallogr D Struct Biol* **79**, 368-373 (2023). https://doi.org/10.1107/S2059798323002413

59.   E. C. Meng *et al.*, UCSF ChimeraX: Tools for structure building and analysis. *Protein Sci* **32**, (2023). https://doi.org/10.1002/pro.4792

60. U. Demmer, O. N. Lemaire, M. Belhamri, U. Ermler, Ethoxylate Polymer-Based 96-Well Screen for Protein Crystallization. *Crystals* **13**, (2023). https://doi.org/10.3390/cryst13101519

61. C. Vonrhein *et al.*, Data processing and analysis with the autoPROC toolbox. *Acta Crystallographica Section D* **67**, 293-302 (2011). https://doi.org/doi:10.1107/S0907444911007773

62. I. J. Tickle *et al.*, STARANISO. Cambridge, United Kingdom: Global Phasing Ltd. 2018. (http://staraniso.globalphasing.org/cgi-bin/staraniso.cgi)

63. B. E. Bricogne G., Brandl M., Flensburg C., Keller P., Paciorek W., Roversi P, Sharff A., Smart O.S., Vonrhein C., Womack T.O. (2017).

64. V. B. Chen *et al.*, MolProbity: all-atom structure validation for macromolecular crystallography. *Acta Crystallographica Section D* **66**, 12-21 (2010). https://doi.org/10.1107/S0907444909042073

65. F. Neese, F. Wennmohs, U. Becker, C. Riplinger, The ORCA quantum chemistry program package. *The Journal of Chemical Physics* **152**, 224108 (2020). https://doi.org/10.1063/5.0004608

66. J. Lee *et al.*, CHARMM-GUI Input Generator for NAMD, GROMACS, AMBER, OpenMM, and CHARMM/OpenMM Simulations Using the CHARMM36 Additive Force Field. *Journal of Chemical Theory and Computation* **12**, 405-413 (2016). https://doi.org/10.1021/acs.jctc.5b00935

67. B. R. Brooks *et al.*, CHARMM: the biomolecular simulation program. *Journal of Computational Chemistry* **30**, 1545-1614 (2009). https://doi.org/10.1002/jcc.21287

68. S. Jo, T. Kim, V. G. Iyer, W. Im, CHARMM-GUI: a web-based graphical user interface for CHARMM. *Journal of Computational Chemistry* **29**, 1859-1865 (2008). https://doi.org/10.1002/jcc.20945

69. J. Huang *et al.*, CHARMM36m: an improved force field for folded and intrinsically disordered proteins. *Nature Methods* **14**, 71-73 (2017). https://doi.org/10.1038/nmeth.4067

70. J. Tao, J. P. Perdew, V. N. Staroverov, G. E. Scuseria, Climbing the density functional ladder: nonempirical meta-generalized gradient approximation designed for molecules and solids. *Physical Review Letters* **91**, 146401 (2003). https://doi.org/10.1103/PhysRevLett.91.146401

71. F. Weigend, R. Ahlrichs, Balanced basis sets of split valence, triple zeta valence and quadruple zeta valence quality for H to Rn: Design and assessment of accuracy. *Physical Cemistry Chemical Physics* **7**, 3297-3305 (2005). https://doi.org/10.1039/b508541a

72. S. Grimme, S. Ehrlich, L. Goerigk, Effect of the damping function in dispersion corrected density functional theory. *Journal of Computational Chemistry* **32**, 1456-1465 (2011). https://doi.org/10.1002/jcc.21759

73. L. R. Maurer, M. Bursch, S. Grimme, A. Hansen, Assessing Density Functional Theory for Chemically Relevant Open-Shell Transition Metal Reactions. *Journal of Chemical Theory and Computation* **17**, 6134-6151 (2021). https://doi.org/10.1021/acs.jctc.1c00659

74. C. Zhao, R. Wu, S. Zhang, X. Hong, Benchmark Study of Density Functional Theory Methods in Geometry Optimization of Transition Metal-Dinitrogen Complexes. *The Journal of Physical Chemistry A* **127**, 6791-6803 (2023). https://doi.org/10.1021/acs.jpca.3c04215

75. J. M. Mouesca, Density functional theory-broken symmetry (DFT-BS) methodology applied to electronic and magnetic properties of bioinorganic prosthetic groups. *Methods in Molecular Biology* **1122**, 269-296 (2014). https://doi.org/10.1007/978-1-62703-794-5_15

76. C. F. Matta, R. J. Boyd, in *The Quantum Theory of Atoms in Molecules*. (2007), pp. 1-34.

77. T. Lu, F. Chen, Multiwfn: a multifunctional wavefunction analyzer. *Journal of Computational Chemistry* **33**, 580-592 (2012). https://doi.org/10.1002/jcc.22885

78. S. F. Altschul, W. Gish, W. Miller, E. W. Myers, D. J. Lipman, Basic local alignment search tool. *Journal of Molecular Biology* **215**, 403-410 (1990). https://doi.org/10.1016/S0022-2836(05)80360-2

79. L. Fu, B. Niu, Z. Zhu, S. Wu, W. Li, CD-HIT: accelerated for clustering the next-generation sequencing data. *Bioinformatics* **28**, 3150-3152 (2012). https://doi.org/10.1093/bioinformatics/bts565

80. F. Sievers *et al.*, Fast, scalable generation of high-quality protein multiple sequence alignments using Clustal Omega. *Molecular Systems Biology* **7**, 539 (2011). https://doi.org/10.1038/msb.2011.75

81. G. E. Crooks, G. Hon, J. M. Chandonia, S. E. Brenner, WebLogo: a sequence logo generator. *Genome Research* **14**, 1188-1190 (2004). https://doi.org/10.1101/gr.849004

Supplementary Materials.
Materials and Methods
Figs. S1 to S27
Tables S1 to S8
References (*46–81*)
Movie S1